 doi:10.20944/preprints202203.0390.v1

3D Printed Engineered, Strain-Hardening Geopolymer Composite (EGC/SHGC) as Permanent Formwork for Concrete Beam Construction

Shin Hau Bong[1], Behzad Nematollahi[1,2*], Viktor Mechtcherine[3], Victor C. Li[4], Kamal H. Khayat[5]

[1] Centre for Smart Infrastructure and Digital Construction, School of Engineering, Swinburne University of Technology, Melbourne, Australia
[2] Department of Civil and Structural Engineering, The University of Sheffield, Sheffield, UK
[3] Institute of Construction Materials, Technische Universität Dresden, Dresden, Germany
[4] Civil and Environmental Engineering, University of Michigan, Ann Arbor, USA
[5] Department of Civil, Architectural and Environmental Engineering, Missouri University of Science and Technology, Rolla, USA

***Corresponding author:** bnematollahi@swin.edu.au

Abstract: The extrusion-based 3D concrete printing (3DCP) technology allows the fabrication of permanent formwork with intricate shapes, into which fresh concrete is cast to build structural members with complex geometry. This significantly enhances the geometric freedom of concrete structures without the use of expensive temporary formwork. In addition, with proper material choice for the permanent formwork, the load-bearing capacity and durability of the resulting structure can be improved. This paper investigates 3DCP of permanent formwork for reinforced concrete (RC) beam construction. A 3D-printable engineered geopolymer composite (3DP-EGC, or strain-hardening geopolymer composite, 3DP-SHGC) recently developed by the authors was used for fabrication of the permanent formwork. The 3DP-EGC exhibits strain-hardening behaviour under direct tension. Two different printing patterns were used for the soffit of the permanent formwork to investigate the effect of this parameter on the flexural performance of RC beams. A conventionally mould-cast RC beam was also prepared as the control beam for comparison purposes. The results showed that the RC beams constructed using the 3DP-EGC permanent formwork exhibited superior flexural performance to the control beam. Such beams yielded significantly higher cracking load (up to 43%), deflection at ultimate load (up to 60%), ductility index (50%) and absorbed energy (up to 107%) than those of the control beam. The ultimate load was comparable with or slightly higher than that of the control beam. Furthermore, the printing pattern at the soffit of the permanent formwork was found to have a significant influence on the flexural performance of the RC beams.

Keywords: 3D concrete printing; engineered geopolymer composite; strain-hardening; permanent formwork; reinforced concrete beam.

1. Introduction

The use of temporary formwork for concrete construction has a significant impact on construction speed, cost and wastage [1, 2]. The cost of formwork is estimated to be about

Preprints (www.preprints.org) | NOT PEER-REVIEWED | Posted: 30 March 2022 doi:10.20944/preprints202203.0390.v1

35%-60% of the overall cost of concrete construction [1]. Formwork is a major source of wastage in construction as it is often made of timber that is eventually discarded. Moreover, the geometric freedom of concrete structures is considerably limited by the formwork shape. Utilising 3D concrete printing (3DCP) technology to manufacture permanent formwork can be a potential solution to tackle the aforementioned issues. Unlike the conventional temporary formwork, the 3D printed concrete permanent formwork serves to mould the fresh concrete to the required shape and dimension and also becomes part of the concrete component, contributing to the final structural capacity of the member throughout the service life of the concrete structure [3]. In addition, the 3D printed concrete permanent formwork with complex geometry can be easily manufactured, which significantly enhances the geometric freedom of concrete structure. With proper material choice for fabrication of the 3D printed concrete permanent formwork, the durability of the resulting structure can also be enhanced when the formwork serves as a protective coating.

Over the past few years, several studies have been conducted on construction of reinforced concrete (RC) column or beam specimens using engineered cementitious composites (ECC, or, using another wide-spread term for this group of materials: strain-hardening cement-based composites, SHCC) or other types of high-performance fibre-reinforced cementitious composites (HPFRCC) as precast permanent formwork [4-10]. For instance, Pan et al. [4] investigated the seismic behaviour of the RC columns produced using precast steel-reinforced ECC/SHCC permanent formwork. The results showed that the RC columns constructed using steel-reinforced ECC/SHCC permanent formwork exhibited higher energy dissipation capacity, shear capacity and ductility compared to those of the conventionally mould-cast RC column under seismic loading conditions. Tian et al. [5] investigated axial behaviour of the RC column constructed using grid-reinforced ultra-high performance concrete (UHPC) as the precast permanent formwork. Carbon fibre reinforced polymer grid and stainless steel gird were used as reinforcement. The results showed that the RC columns made with the precast grid-reinforced UHPC permanent formwork exhibited higher axial load carrying capacity and stiffness in comparison to those of the conventionally mould-cast RC column. However, the ductility and crack resistance of the RC column decreased due to the brittle nature of UHPC. The authors reported that the use of carbon fibre reinforced polymer grid could improve the ductility and toughness of the RC column as compared to stainless steel grid.

The effects of surface treatment of permanent formwork on the mechanical performance of structural elements have been studied. Leung and Cao [8] investigated the flexural performance of concrete beams constructed using ECC/SHCC as the precast permanent formwork with different surface treatments. The results showed that the beams constructed using the ECC/SHCC permanent formwork with transverse grooves along the surface exhibited significantly higher flexural capacity than that of the beam fabricated using the ECC/SHCC permanent formwork with smooth surface. Zhang et al. [7] studied the shear behaviour of the RC beams without shear reinforcement constructed using precast ECC/SHCC permanent formwork. Three different surface conditions, namely smooth interface, anchored interface and rugged interface, were prepared to investigate the interface bond strength between ECC/SHCC permanent formwork and concrete core. The authors reported that the RC beam constructed

Preprints (www.preprints.org) | NOT PEER-REVIEWED | Posted: 30 March 2022 doi:10.20944/preprints202203.0390.v1

using ECC/SHCC permanent formwork significantly improved the shear and deformation capacities compared to those of the conventionally mould-cast RC beam without shear reinforcement. The authors also reported that the ECC/SHCC permanent formwork with rugged interface exhibited the highest interface bond strength compared to that with smooth interface and anchored interface. The interface bond strength between the ECC/SHCC permanent formwork and concrete core was found to have limited correlation to the shear capacity of the RC beams.

Recently, some studies have been conducted to build RC structures using 3D printed concrete permanent formwork [11-13]. Vantyghem et al. [11] manufactured and tested a 4-m long topology optimised post-tensioned concrete girder constructed using 3D printed hollow girder segments. The girder segments were produced using a 3D printable ordinary Portland cement (OPC)-based mortar. The printed girder segments and post-tensioning cables were assembled, and a shrinkage compensating high-strength mortar was then used to fill the hollow interior of the post-tensioning cables. Finally, a post-tension force of 50 kN was applied. The authors reported that the topology optimised beam made of 3D printed girder segments saved nearly 20% volume of concrete when compared to the conventional beam constructed having a T-section girder with the same dimensions and total deflection. Anton et al. [12] manufactured nine 2.7-m high columns with complex geometry and surface texture. The hollow permanent formwork was 3D printed using an OPC-based mortar. Subsequently, a conventional steel reinforcement cage was placed in the printed permanent formwork, followed by casting of fresh concrete. In another study, Zhu et al. [13] investigated the structural perfomance of the RC columns under compression. The 3D printed permanent formwork for the columns was made using a 3D printable OPC-based mortar, which contained 6 mm long polyethylene fibres and calcium carbonate whisker to reduce shrinkage and enhance the micro-mechanical performance of the print material. Subsequently, the convetional steel reinforcement cages with three different longitudinal steel reinforcement ratios (0.0%, 1.9% and 2.5%) were placed inside the printed permanent formwork, and fresh concrete was cast into it. The conventional mould-cast RC columns with the same reinforcement ratios were also manufactured for comparison. The results showed that the load bearing capacity and stiffness of the RC column made with the 3D printed permanent formwork were higher in comparison to those of the control RC columns. This was due to the higher strength of the printable mortar used for manufacturing the permanent formwork as compared to the cast-in-place concrete (40 MPa compared to 30 MPa), as well as the higher confinement effect from the printed permanent formwork. Furthermore, the authors reported that good bonding was observed at the interface of the concrete core and the printed permanent formwork.

It should be noted that the aforementioned 3D printed concrete permanent formwork were manufactured using 3D printed OPC-based mortars, which have very limited or no contribution to the final load bearing capacity and crack control of the concrete structure. In addition, OPC was used as the main binder in the mixture compositions, which compromises the sustainability credentials of 3DCP due to the high carbon emissions and embodied energy associated with OPC production [14, 15]. Therefore, the study at hand aims to investigate the performance of RC beams constructed using permanent formwork made of a 3D-printable engineered

Preprints (www.preprints.org) | NOT PEER-REVIEWED | Posted: 30 March 2022 doi:10.20944/preprints202203.0390.v1

geopolymer composite (3DP-EGC, or strain-hardening geopolymer composite, 3DP-SHGC). The authors recently developed a 3DP-EGC. Similar to 3D-printable ECC (3DP-ECC or 3DP-SHCC), the 3DP-EGC shows strain-hardening behaviour under uniaxial tension [16]. However, the environmental footprint of the 3DP-EGC is significantly lower than that of 3DP-ECC, as the 3DP-EGC is made of geopolymer. Geopolymer utilises industrial waste materials such as fly ash and slag and does not contain any OPC, thereby reducing the carbon emissions by as much as 80% [17]. In addition, EGC exhibits superior sulphuric acid resistance to ECC [18]. Two permanent formwork systems with different printing patterns were manufactured using the 3DP-EGC. The flexural performance of the RC beams constructed with the permanent formwork was evaluated by conducting four-point bending tests. The results were also compared with those of the conventionally mould-cast RC beam.

2. Properties of 3DP-EGC and concrete for casting of RC beams

The 3DP-EGC mixture developed in the authors' previous study [16] was used to print the permanent formwork in this investigation. The details of the 3DP-EGC mixture including the mixture proportion, printing performances, rheological and mechanical properties were presented and discussed in [16]. The key mechanical properties of the 3DP-EGC and its counterpart mould-cast EGC at 28 days are given in **Table 1**.

The concrete used in this study for casting of the RC beam specimens was a conventional OPC concrete with a target characteristic compressive strength exceeding of 40 MPa at 28 days and had a maximum nominal aggregate size of 14 mm. The slump test performed before casting of the RC beam specimens yielded a value of approximately 130 mm. Twelve concrete cylinders (100 mm diameter × 200 mm height) were produced during casting of the RC beam specimens to determine compressive strength of the concrete. Compression test on the concrete cylinders was conducted on the same day as the bending tests. The density of each concrete cylinder was determined by weighting the air-dried specimens before the compression test. The average compressive strength (f_{cm}) and density (ρ) of the concrete were 44.6 ± 2.2 MPa and 2395 ± 16 kg/m^3, respectively. According to AS 1379 [19], the characteristic compressive strength of the concrete (f_c') at 28 days was calculated to be 41.5 MPa.

3. Experimental procedures

3.1 Details of beam specimens

As shown in **Figure 1**, all beam specimens had a 200 mm × 300 mm (W × D) rectangular cross-section and a length of 1800 mm. The tensile reinforcements were 2N20 (i.e., two 20 mm ribbed steel bars with yield stress (f_{sy}) of 500 MPa). The compressive reinforcements were 2N10 (i.e., two 10 mm ribbed steel bars with f_{sy} of 500 MPa). To avoid shear failure prior to flexural failure, stirrups made of 12 mm ribbed steel bars (with f_{sy} of 500 MPa) were placed 100 mm centre-to-centre with a cover of 25 mm.

The flexural load bearing capacity and shear capacity of the conventionally mould-cast RC beam with the aforementioned reinforcement were estimated in accordance with AS 3600 [20], as shown in Appendix A. Using the calculated ultimate shear capacity (V_u) value (see Appendix

Preprints (www.preprints.org) | NOT PEER-REVIEWED | Posted: 30 March 2022 doi:10.20944/preprints202203.0390.v1

A) as the applied shear force, the applied bending moment was calculated to be 259.0 kN·m, which was much higher than the ultimate moment capacity (M_u) of the RC beam (71.9 kN·m). Therefore, the RC beam would fail in flexural mode rather than in shear mode. In addition, the cracking moment (M_{cr}) of the mould-cast RC beam was calculated to be 12.9 kN·m.

3.2 3D printing process and testing of specimens

A gantry-type 3DCP machine was used in this study. A detailed description of the printer can be found in [21]. A 20 mm circular nozzle was used for printing the permanent formwork. The dimensions of the formwork are schematically illustrated in **Figure 2**. Two different printing patterns (**Figure 3**) for the soffit (i.e., tension region) of the permanent formwork were designed and used to investigate the effect of this parameter on the flexural performance of the RC beam. The RC beam made using the 3DP-EGC permanent formwork with Type A printing pattern was denoted as Type A beam, while the beam made using the 3DP-EGC permanent formwork with Type B printing pattern was denoted as Type B beam. The printing speed and extrusion rate were 25 mm/s and ~0.75 L/min, respectively. After printing, the 3DP-EGC permanent formwork systems were covered with a plastic sheet and left in the laboratory environment at room temperature (23 ± 3℃).

After 21 days of ambient temperature curing, the reinforcement cages were placed inside the printed formwork, and the OPC concrete was cast (**Figure 4**). The conventionally mould-cast RC beam (i.e., the control cast-in place beam) with the same dimensions was also prepared using temporary formwork for comparison purposes. Subsequently, all RC beam specimens were covered with a plastic sheet and left in the laboratory environment at room temperature until testing. All specimens were tested after 28 days of age.

The flexural performance of the RC beam specimens was evaluated by conducting four-point bending tests; **Figure 5** shows schematically the test setup. All specimens were tested with the mid-span measuring 400 mm under displacement control at the rate of 0.5 mm/min. A linear variable differential transformer (LVDT) was used to determine the mid-span deflection, and two more LVDTs were used to monitor the vertical displacement at the supports. The resulting force versus mid-span deflection curves are presented in Section 4.

3.3 Flexural capacity of RC beam made with 3DP-EGC permanent formwork

Similar to the calculation of M_{cr} of the conventionally mould-cast RC beam presented in Appendix A, the M_{cr} of the RC beam specimens produced using the 3DP-EGC permanent formwork was calculated by transforming the 3DP-EGC permanent formwork sections to an equivalent area of concrete as schematically illustrated in **Figure 6**. It should be noted that the anisotropic behaviour due to 3D printing process is ignored in the following calculations. In other words, only for the purpose of this calculation, the 3DP-EGC permanent formwork is assumed to be a mould-cast EGC permanent formwork. In addition, it is assumed that the steel reinforcement in compressive region has a negligible effect on the M_{cr}. **Table 2** presents the material characteristics of the concrete, the EGC and steel reinforcement used for calculation of the M_{cr} of the cross-section. The calculation procedure to determine the M_{cr} of RC beam

Preprints (www.preprints.org) | NOT PEER-REVIEWED | Posted: 30 March 2022 doi:10.20944/preprints202203.0390.v1

specimens made using the 3DP-EGC permanent formwork is summarised in Appendix B. Based on the calculations presented in Appendix B, the M_{cr} of the RC beam specimens made using the 3DP-EGC permanent formwork was calculated to be 16.9 kN.m.

The M_u of the RC beam specimens made using the 3DP-EGC permanent formwork can be calculated using the equilibrium equations. The corresponding stress and strain diagrams for the cross-section are presented in **Figure 7**. It is assumed that the steel is in yield condition, while the steel reinforcement in compressive region has negligible effect on the M_u. The anisotropic behaviour due to 3D printing process is also ignored. **Table 3** presents the material characteristics of the EGC used for calculation of the M_u of the cross-section. The calculation procedure to determine the M_u of RC beam specimens made using the 3DP-EGC permanent formwork is presented in Appendix B. Based on the calculations presented in Appendix B, the M_u of the RC beam specimens constructed using the 3DP-EGC permanent formwork was calculated to be 78.8 kN·m.

4. Results and discussions

Figure 8 presents the force vs. mid-span deflection curves of all RC beam specimens. As shown in **Figure 8b**, after reaching the yielding force both Type A and Type B beams exhibited deflection-hardening behaviour, while the control beam showed typical deflection-softening behaviour. **Table 4** summarises the cracking force (P_{cr}), yielding force (P_y), ultimate force (P_{ult}) and the corresponding deflection values of all RC beam specimens. In both Type A and Type B beams, the P_{cr} values and their corresponding deflection values (δ_{cr}) were higher than those of the control beam. The P_{cr} and δ_{cr} of Type A beam were 11% and 20% higher than those of the control beam, respectively. The corresponding values for Type B beam were 43% and 40%, respectively. When comparing the results obtained for Type A and Type B beams, the P_{cr} and δ_{cr} of Type B beam were 29% and 17% higher than those of Type A beam, respectively. This is because in Type B beam the tensile stresses are parallel to the printing direction, where the tensile ductility of EGC contributes to higher extent to the cracking resistance of the beam, while in Type A beam the tensile stresses are perpendicular to the printing direction of the filaments at the soffit of the formwork. Therefore, the resistance of Type A beam to cracking is mainly governed by the bond strength of the adjacent printed filaments, which is generally weaker compared to the strength of the printed filaments.

The P_y and its corresponding deflection (δ_y) of the RC beam specimens were well comparable as identical steel reinforcement was used in all RC beams. As shown in **Table 4**, the P_{ult} of Type A beam was comparable with that of the control beam; however, the deflection at the ultimate load (δ_{ult}) was 59% higher than that of the control beam. The P_{ult} and δ_{ult} of Type B beam were 5% and 60%, respectively, higher than those of the control beam. The significantly higher δ_{ult} of Type A and Type B beams is attributed to the strain-hardening of the 3DP-EGC layers at the soffit of the permanent formwork. It should be noted that the P_{ult} of Type B beam was slightly higher (5%) than that of the Type A beam. This is due to the higher fibre bridging efficiency of 3DP-EGC in Type B beam as the tensile stresses are parallel to the printing direction in this beam.

Preprints (www.preprints.org) | NOT PEER-REVIEWED | Posted: 30 March 2022 doi:10.20944/preprints202203.0390.v1

Using the M_{cr} and M_u values calculated in Sections 3.1.1 and 3.3, the calculated cracking force ($P_{cr.cal}$) and ultimate force ($P_{ult.cal}$) of all RC beam specimens are summarised and compared with the test results in **Table 5**. It should be noted that the $P_{cr.cal}$ and $P_{ult.cal}$ values are based on theoretical calculations for comparison purposes only, and not aimed to be used for prediction. It can be seen that the P_{cr} and $P_{cr.cal}$ values of the control beam were comparable (i.e., $P_{cr}/P_{cr.cal}$ = 0.96). Similar to the control beam, the P_{cr} and $P_{cr.cal}$ values of Type B beam were also comparable (i.e., $P_{cr}/P_{cr.cal}$ of 1.05). However, the P_{cr} value of Type A beam was lower than its $P_{cr.cal}$ value (i.e., $P_{cr}/P_{cr.cal}$ = 0.81). This is because the 3DP-EGC permanent formwork is assumed to be a quasi mould-cast EGC permanent formwork in the calculations. In addition, in Type A beam the cracking was initiated at the interfaces between printed filaments, which are generally weaker compared to the strength of the printed filaments. The cracking patterns of the RC beams are discussed in the following paragraphs. As shown in **Table 5**, the P_{ult} values of all RC beam specimens were comparable with their corresponding $P_{ult,cal}$ values. The ratios of $P_{ult}/P_{ult.cal}$ of the control beam, Type A beam and Type B beam were equal to 1.08, 0.99 and 1.04, respectively.

Table 6 presents the ductility index and absorbed energy of all RC beams. This index gives δ_{ult}/δ_y, i.e., the ratio of deflection at ultimate force to deflection at yielding force. The absorbed energy of the RC beam specimens was calculated from the area under the load vs. mid-span deflection curves (see **Figure 8a**) up to the mid-span deflection corresponding to P_{ult}. As shown in **Table 6**, the ductility indices of both Type A and Type B beams were identical and 50% higher than that of the control beam. This is due to the significantly higher δ_{ult} of Type A and Type B beams. Similar to the ductility index, the absorbed energy values of Type A and Type B beams were 94% and 107% higher than that of the control beam, respectively. The absorbed energy of Type B beam was about 7% higher than that of Type A beam, which is due to the higher ultimate force of Type B beam (see **Table 4**). The significantly higher ductility index and absorbed energy of Type A and Type B beams (constructed using the 3DP-EGC permanent formwork) clearly shows their superior flexural performance to the conventionally mould-cast RC beam specimen.

Figures 9 to **11** show the cracking patterns of the control beam, Type A and Type B beams at the ultimate loads, respectively. It should be noted that white paint was sprayed on the specimens before conducting the four-point bending tests to obtain clear visible cracks. **Figure 9 a** shows a typical cracking pattern of flexural failure of the conventionally mould-cast RC beam. The flexural cracks initiated from the bottom (tension region) of the beam and propagated toward the two loading points (see **Figure 9 b,c**) as the load increased. In addition, several inclined cracks were observed along the shear span; see **Figure 9 d,e**.

For Type A beam, a single large crack accompanied by multiple fine cracks were observed at the bottom of the beam; see **Figure 10 d**. It should be pointed out that these cracks developed at the interfaces between printed filaments; see **Figure 10 c,d**. This can be traced back to fact that the bond strength between the adjacent printed filaments is weak compared to the strength of the printed filaments. As the load increased, the existing large crack propagated toward the two loading points. However, the crack did not propagate as far from the bottom of the beam

Preprints (www.preprints.org) | NOT PEER-REVIEWED | Posted: 30 March 2022 doi:10.20944/preprints202203.0390.v1

as in the control beam, and multiple fine cracks developed in the 3DP-EGC permanent formwork; see **Figure 10 b-e**. In contrast, in Type B beam significant number of fine cracks were observed in the tension region at the ultimate load; see **Figure 11 b-e**. The cracking behaviour observed in Type B beam is very beneficial for improving the cracking resistance and durability of the RC beam as multiple micro-cracks (with widths typically below 100 μm) can significantly delay the transport of aggressive agents (e.g., chlorides) to steel bars [23].
Figures 12 to **14** show the cracking pattern of the control beam, Type A beam and Type B beam at 16 mm mid-span deflection, respectively. It should be noted that all RC beam specimens exhibited deflection-softening at mid-span deflection of 16 mm. **Figure 12a** shows that in the control beam the cracks at the mid-span significantly widened as the deflection increased. In addition, the concrete crushing in the compression zone (i.e., between two loading points) of the control beam was observed; see **Figure 12a**. In Type A beam, the large crack shown in **Figure 13d** was widely opened and propagated towards the compressive region as the deflection increased, while in Type B beam, the existing fine cracks shown in **Figure 14d** developed into a larger crack that propagated towards the compressive region as the deflection increased.

Figure 15 shows the cracking pattern of the bottom side of all RC beams after unloading. Multiple fine cracks were observed on the bottom side of the control beam and Type A beam; however, only a single large crack was observed on the bottom side of Type B beam. These observations demonstrated that the printing pattern of the formwork base has a significant influence on the cracking pattern of the RC beam constructed using the 3DP-EGC permanent formwork.

Similar to the control beam, concrete crushing in the compression zone of both Type A and Type B beams was observed (**Figure 16)**. It is interesting to note that in Type A and Type B beams, concrete crushing in the compression zone was not observed on the 3DP-EGC permanent formwork; cf. **Figure 12a** with **Figure 13a** and **Figure 14a**. It was also noted that in the compression zone the 3DP-EGC permanent formwork was de-bonded from the cast concrete at the mid-span of the beams (**Figure 16)**.

5. Conclusions

This paper evaluates the behaviour and performance of 3DP-EGC permanent formwork for RC beams. Two different printing patterns were used at the soffit of the permanent formwork to investigate the effect of printing direction on the flexural performance of RC beams. The results were compared with those obtained for a conventionally mould-cast RC beam (i.e., the control beam). Based on the experimental results, the following conclusions are drawn:

(1) The RC beams made using the 3DP-EGC permanent formwork exhibited superior flexural performance in comparison to the control beam. In addition, the experimental results indicate that the interface between the printed permanent formwork and concrete core did not initiate any premature failure.

Preprints (www.preprints.org) | NOT PEER-REVIEWED | Posted: 30 March 2022 doi:10.20944/preprints202203.0390.v1

(2) The RC beams produced using the 3DP-EGC permanent formwork exhibited significantly higher cracking load (up to 43%), deflection at the ultimate load (up to 60%), ductility index (50%), and absorbed energy (up to 107%) than those of the control beam. However, the ultimate flexural load capacity for the RC beams made using the 3DP-EGC permanent formwork was not significantly higher than that of the control beam.

(3) After steel yielding, both beams with 3DP-EGC permanent formwork (Type A and B have printed filament perpendicular and parallel, respectively, to the principle tensile stress on the bottom of beam) exhibited deflection-hardening behaviour, while the control beam showed typical deflection-softening behaviour. The ability of the ductile EGC in the permanent formwork to continue sharing load with steel beyond yielding contributes to the superior performance of beams with 3DP-EGC permanent formwork. In contrast, the cracked concrete in the control beams gave up carrying tensile forces at this stage of loading.

(4) The printing pattern at the soffit of the permanent formwork was found to have significant influence on the flexural performance of the RC beams. For Type A beam, the cracking initiated at the interfaces between printed filaments and was accompanied by multiple fine cracks as the load increased. In the case of Type B beam, significant number of fine cracks were observed in the tension region and ultimately developed into a larger crack that propagated towards the compressive zone as the deflection increased. The formation of multiple fine crack with tight crack width is very beneficial for improving the durability of the RC beam, as they can significantly delay the transport of aggressive agents (e.g., chlorides) to steel bars.

Appendix A

According to AS 3600 [20], the ultimate moment capacity M_u of the conventionally mould-cast RC beam shall be calculated from the following equation:

$$M_u = A_{st} f_{sy} d \left[1 - \frac{A_{st} f_{sy}}{2\alpha_2 b d f_c'}\right] \quad \text{(A.1)}$$

Preprints (www.preprints.org) | NOT PEER-REVIEWED | Posted: 30 March 2022 doi:10.20944/preprints202203.0390.v1

where A_{st} is the area of steel reinforcement in the tension region, d is the effective depth of the section and b is the width of the section. According to Clause 8.1.3 of AS 3600 [20], α_2 shall be determined from Eq. (A.2):

$$\alpha_2 = 0.85 - 0.0015f_c' \quad \text{(A.2)}$$

Using Equation (A.1), the M_u of the mould-cast RC beam was calculated to be 71.9 kN·m. According to Clause 8.1.5 of AS 3600 [20], k_u shall be ≤ 0.36 to ensure adequate ductility of the beam is attained. In this regard, k_u shall be calculated from Eq. (A.3):

$$k_u = \frac{A_{st}f_{sy}}{\alpha_2\gamma bdf_c'} \quad \text{(A.3)}$$

where γ shall be determined from Eq. (A.4):

$$\gamma = 0.97 - 0.0025f_c' \quad \text{(A.4)}$$

The calculated k_u value was 0.22, which was less than 0.36. Thus, the beam satisfied this requirement as per Clause 8.1.5 of AS 3600 [20].

The cracking moment M_{cr} of the conventionally mould-cast RC beam can be calculated by transforming and replacing the steel section in the cross-section to an equivalent area of concrete. It should be noted that the steel reinforcement in compressive region is assumed to has negligible effect on M_{cr}. The following equation was used to calculate M_{cr}:

$$M_{cr} = \frac{f_{ct,f}'I_u}{D-d_n} \quad \text{(A.5)}$$

where $f_{ct,f}'$ is the characteristic flexural tensile strength of the concrete, which is equal to $0.6\sqrt{f_c'}$ as per Clause 3.1.1.3 of AS 3600 [20], I_u is the gross section second moment of area in uncracked state and was calculated to be 4.823×10^8 mm^4, D is the depth of the section (300 mm), and d_n is the depth of neutral axis which can be calculated from Eq. (A.6):

$$d_n = \frac{bD\times\frac{D}{2}+(n-1)A_{st}d}{bD+(n-1)A_{st}} \quad \text{(A.6)}$$

where $n = \frac{E_s}{E_c}$ that is also known as the modular ratio, and E_s is the steel modulus of elasticity that is equal to 200000 MPa; E_c is the concrete modulus of elasticity and shall be calculated from the following equation as per Clause 3.1.2 of AS 3600 [20]:

$$E_c = (\rho^{1.5}) \times (0.024\sqrt{f_{cmi}} + 0.12) \quad \text{(A.7)}$$

Preprints (www.preprints.org) | NOT PEER-REVIEWED | Posted: 30 March 2022 doi:10.20944/preprints202203.0390.v1

where ρ is the density of concrete and f_{cmi} is equal to 90% of f_{cm} in accordance with Clause 3.1.1.2 of AS 3600 [20]. Using Equation (A.7), the M_{cr} of the mould-cast RC beam was calculated to be 12.9 kN·m.

The ultimate shear capacity V_u of the mould-cast RC beam was calculated in accordance with AS 3600 [20] as follows:

$$V_u = V_{uc} + V_{us} \quad \text{(A.8)}$$

$$V_{uc} = k_v\sqrt{f_c'}bd_v \quad \text{(A.9)}$$

$$V_{us} = \frac{A_{sv}f_{sy}d_v}{s}\cot(\theta_v) \quad \text{(A.10)}$$

where V_{uc} is the shear capacity contributed by concrete, and V_{us} is the shear capacity contributed by shear reinforcement. The effective shear depth of the section d_v was determined as the greater of 0.72D or 0.9d. According to Clause 8.2.4.3 of AS 3600 [20], the k_v value shall be taken as 0.15 by assuming $\frac{A_{sv}}{s} \geq \frac{A_{sv.min}}{s}$ and the θ_v value shall be taken as 36°. The area of shear reinforcement A_{sv} was calculated to be 226.2 mm^2, and the centre-to-centre spacing of shear reinforcement s was 100 mm. By substituting the aforementioned values in Eqs. (A.8), (A.9) and (A.10), the V_u of the mould-cast concrete beam was calculated to be 398.5 kN.

To verify the initial assumption of $\frac{A_{sv}}{s} \geq \frac{A_{sv.min}}{s}$, the minimum area of shear reinforcement ($A_{sv.min}$) shall be calculated from the following equation as per Clause 8.2.1.7 of AS 3600 [20]:

$$\frac{A_{sv.min}}{s} = \frac{0.08\sqrt{f_c'}b}{f_{sy}} \quad \text{(A.11)}$$

Using Eq. (A.11), the $\frac{A_{sv.min}}{s}$ was calculated to be 0.2 which was much smaller than the $\frac{A_{sv}}{s}$ = 2.3. Hence, the initial assumption was correct. In addition, the spacing of shear reinforcement provided shall be smaller than the maximum spacing s_{max}, which shall be determined as the lesser of 300 mm or 0.5D as per Clause 8.3.2.2 of AS 3600 [20]. The s_{max} was determined to be 150 mm that was greater than the spacing provided for the shear reinforcement (100 mm).

Appendix B

The cracking moment M_{cr} of the RC beam specimens produced using the 3DP-EGC permanent formwork was calculated by transforming the 3DP-EGC permanent formwork sections to an equivalent area of concrete as schematically illustrated in **Figure 6**.

The equivalent area of concrete to replace the area of steel ($(n-1)A_{st}$) is:

Preprints (www.preprints.org) | NOT PEER-REVIEWED | Posted: 30 March 2022 doi:10.20944/preprints202203.0390.v1

$n = \frac{E_s}{E_c} = 6.3$
$(n-1)A_{st} = 3313\ \text{mm}^2$

The equivalent area of concrete to replace the area of 3DP-EGC permanent formwork (nA_{EGC}) is determined as follows:

$n = \frac{E_{EGC}}{E_c} = 0.56$
$nA_{EGC} = 2A_1 + A_2 = 18750\ \text{mm}^2$
$A_2 = 3750\ \text{mm}^2$
$A_1 = \frac{nA_E - A_2}{2} = 3369\ \text{mm}^2$
$b'' = \frac{A_2}{D} = 11.2\ \text{mm}$

The depth of neutral axis (d_n) is:

$$d_n = \frac{b'D' \times \frac{D'}{2} + (n-1)A_{st}d + 2A_1 \times \frac{D}{2} + A_2 \times \frac{t}{2}}{b'D' + (n-1)A_{st} + 2A_1 + A_2} = 137.5\ \text{mm}$$

The gross section second moment of area (I_u) in uncracked state is calculated as follows:

$$I_u = \frac{b'D'^3}{12} + b'D' \times \left(\frac{D'}{2} - d_n\right)^2 + (n-1)A_{st}(d-d_n)^2 + \frac{b't^3}{12} + b't \times \left(\left(\frac{t}{2} + D'\right) - d_n\right)^2 + 2\left[\frac{b''D^3}{12} + b'D \times \left(\frac{D}{2} - d_n\right)^2\right]$$
$$= 440.38 \times 10^6\ \text{mm}^4$$

Using the $f'_{ct,f}$ of EGC (adopted from [16]) and Equation (A.5), the M_{cr} of the RC beam specimens made using the 3DP-EGC permanent formwork was calculated to be 16.9 kN·m.

The ultimate moment capacity M_u of the RC beam specimens made using the 3DP-EGC permanent formwork can be calculated using the equilibrium equations. The corresponding stress and strain diagrams for the cross-section are presented in **Figure 7**. Based on **Figure 7**, the following equations for the forces acting on the cross-section can be written:

$$C = C_c + C_E = 0.85 \times \left[\frac{150}{200} \times f'_c + \frac{50}{200} \times \frac{f'_{CEk}}{\gamma_c}\right] \times d_n \times 200 \quad \text{(B.1)}$$
$$T_S = f_{sy} \times A_s \quad \text{(B.2)}$$
$$T_{E1} = \frac{f_{ultk}}{\gamma_c} \times 25 \times 200 \quad \text{(B.3)}$$
$$T_{E2} = \frac{f_{ultk}}{\gamma_c} \times 50 \times (275 - d_n) \quad \text{(B.4)}$$

By substituting the material characteristics of the concrete, steel and EGC, Equations (B.1), (B.2), (B.3) and (B.4) can be re-written / calculated as follows:

$$C = 7101 d_n\ \text{N} \quad \text{(B.5)}$$

Preprints (www.preprints.org) | NOT PEER-REVIEWED | Posted: 30 March 2022 doi:10.20944/preprints202203.0390.v1

$$T_S = 314200\ \text{N} \quad \text{(B.6)}$$
$$T_{E1} = 12444\ \text{N} \quad \text{(B.7)}$$
$$T_{E2} = 124.4(275 - d_n)\text{N} \quad \text{(B.8)}$$

The depth of the neutral axis d_n can be determined based on force equilibrium equation ($T_S + T_{E1} + T_{E2} - C = 0$). The C and T_{E2} can be calculated once the d_n is determined. Subsequently, the M_u of the cross-section can be obtained by taking moment at the top extreme fibre as follows:

$$M_u = -C \times \frac{d_n}{2} + T_S \times 253 + T_{E1} \times 287.5 + T_{E2} \times \left(\frac{275-d_n}{2} + d_n\right) \quad \text{(B.9)}$$

By substituting the values of C, T_S, T_{E1}, T_{E2}, and d_n into the Equation (B.9), the M_u of the RC beam specimens constructed using the 3DP-EGC permanent formwork was calculated to be 78.8 kN·m.

To verify the initial assumption of the steel is in yield condition, the strain of the steel in the tension region ε_s shall be > ε_{sy} = 0.0025 for the steel reinforcement used in this study. From the strain diagram (see **Figure 7**), ε_s can be determined from Eq. (B.10):

$$\varepsilon_s = (253 - d_n) \times \frac{\varepsilon_C + \varepsilon_E}{d_n} \quad \text{(B.10)}$$

where $\varepsilon_C + \varepsilon_E$ is taken as 0.003. Using Eq. (B.10), the ε_s was calculated to be 0.0122, which was much larger than ε_{sy} = 0.0025. Hence, the initial assumption of yielding of the steel was correct.

Acknowledgements

The authors acknowledge the support from the Australian Research Council Discovery Project DP210101680, Discovery Early Career Researcher Award DE180101587 and Linkage Infrastructure Grant LE170100168, as well as the funding received under the 2018 Australia–Germany Joint Research Co-operation Scheme funded by Universities Australia and German Academic Exchange Service. The first two authors also acknowledge the comments received from Professor Jay Sanjayan at Swinburne University of Technology for designing the cast reinforced concrete beam and for reviewing initial draft of the manuscript.

References

[1] D.W. Johnston, Design and construction of concrete formwork, in: E.G. Nawy (Ed.), Concrete Construction Engineering Handbook, CRC press, New Jersey, Boca Raton, 2008, pp. 7.1-7.48.

[2] K.N. Jha, Formwork for concrete structures, Tata McGraw Hill Education Private Limited 2012.

[3] R. Wringley, Permanent Formwork in Construction (CIRIA C558), CIRIA/Concrete Society (2001) 13-16.

[4] Z. Pan, Y. Zhu, Z. Qiao, S. Meng, Seismic behavior of composite columns with steel reinforced ECC permanent formwork and infilled concrete, Eng. Struct. 212 (2020) 110541.

[5] H. Tian, Z. Zhou, Y. Zhang, Y. Wei, Axial behavior of reinforced concrete column with ultra-high performance concrete stay-in-place formwork, Eng. Struct. 210 (2020) 110403.

[6] B.-T. Huang, Q.-H. Li, S.-L. Xu, C.-F. Li, Development of reinforced ultra-high toughness cementitious composite permanent formwork: Experimental study and Digital Image Correlation analysis, Compos. Struct. 180 (2017) 892-903.

[7] R. Zhang, P. Hu, X. Zheng, L. Cai, R. Guo, D. Wei, Shear behavior of RC slender beams without stirrups by using precast U-shaped ECC permanent formwork, Construct. Build. Mater. 260 (2020) 120430.

[8] C.K.Y. Leung, Q. Cao, Development of pseudo-ductile permanent formwork for durable concrete structures, Mater. Struct. 43(7) (2010) 993-1007.

[9] H. Li, C.K.Y. Leung, S. Xu, Q. Cao, Potential use of strain hardening ECC in permanent formwork with small scale flexural beams, J. Wuhan Univ. Technol. Mater. Sci. Ed. 24(3) (2009) 482-487.

[10] Z. Qiao, Z. Pan, W. Xue, S. Meng, Experimental study on flexural behavior of ECC/RC composite beams with U-shaped ECC permanent formwork, Front. Struct. Civ. Eng. 13(5) (2019) 1271-1287.

[11] G. Vantyghem, W. De Corte, E. Shakour, O. Amir, 3D printing of a post-tensioned concrete girder designed by topology optimization, Autom. Constr. 112 (2020) 103084.

[12] A. Anton, P. Bedarf, A. Yoo, B. Dillenburger, L. Reiter, T. Wangler, R.J. Flatt, Concrete Choreography: Prefabrication of 3D-Printed Columns, Fabricate 2020 (2020) 286-293.

[13] B. Zhu, B. Nematollahi, J. Pan, Y. Zhang, Z. Zhou, Y. Zhang, 3D concrete printing of permanent formwork for concrete column construction, Cement Concr. Compos. 121 (2021) 104039.

 doi:10.20944/preprints202203.0390.v1

[14] D.N. Huntzinger, T.D. Eatmon, A life-cycle assessment of Portland cement manufacturing: comparing the traditional process with alternative technologies, J. Clean. Prod. 17(7) (2009) 668-675.
[15] M. Taylor, C. Tam, D. Gielen, Energy efficiency and CO_2 emissions from the global cement industry, Korea 50(2.2) (2006) 61-67.
[16] S.H. Bong, B. Nematollahi, V.N. Nerella, V. Mechtcherine, Method of formulating 3D-printable strain-hardening geopolymer composites for additive construction, Submitted to Cement Concr. Compos.
[17] P. Duxson, J.L. Provis, G.C. Lukey, J.S. Van Deventer, The role of inorganic polymer technology in the development of 'green concrete', Cement Concr. Res. 37(12) (2007) 1590-1597.
[18] M. Ohno, V.C. Li, Sulfuric acid resistance of strain hardening fiber reinforced geopolymer composite, Indian Concr. J. (2019).
[19] AS 1379:2007, Specification and supply of concrete, Standards Australia, Australia.
[20] AS 3600:2018, Concrete structures, Standards Australia, Australia.
[21] S.H. Bong, M. Xia, B. Nematollahi, C. Shi, Ambient temperature cured 'just-add-water' geopolymer for 3D concrete printing applications, Cement Concr. Compos. 121 (2021) 104060.
[22] Recommendations for design and construction of high performance fiber reinforced cement composites with multiple fine cracks (HPFRCC), Concrete Engineering Series No. 82, Japan Society of Civil Engineers, Japan, 2008.
[23] V.C. Li, Durability of Engineered Cementitious Composites (ECC) and Reinforced ECC (R/ECC) Structural Members, in: V.C. Li (Ed.), Engineered Cementitious Composites (ECC): Bendable Concrete for Sustainable and Resilient Infrastructure, Springer Berlin Heidelberg, Berlin, Heidelberg, 2019, pp. 225-260.

Preprints (www.preprints.org) | NOT PEER-REVIEWED | Posted: 30 March 2022 doi:10.20944/preprints202203.0390.v1

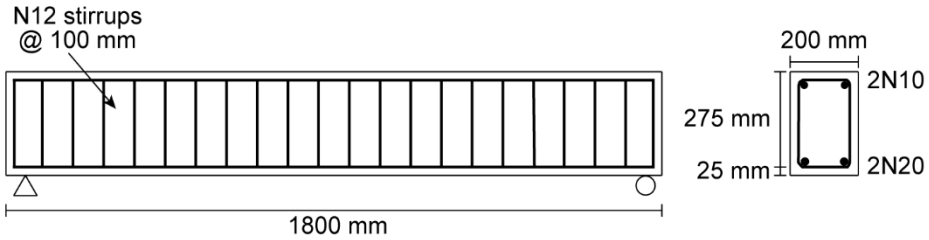

Figure 1. Dimensions and reinforcement detailing of RC beam specimens.

Preprints (www.preprints.org) | NOT PEER-REVIEWED | Posted: 30 March 2022 doi:10.20944/preprints202203.0390.v1

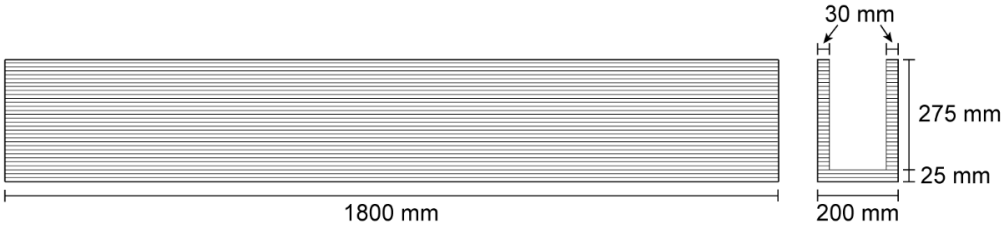

Figure 2. Dimensions of 3DP-EGC permanent formwork.

Preprints (www.preprints.org) | NOT PEER-REVIEWED | Posted: 30 March 2022 doi:10.20944/preprints202203.0390.v1

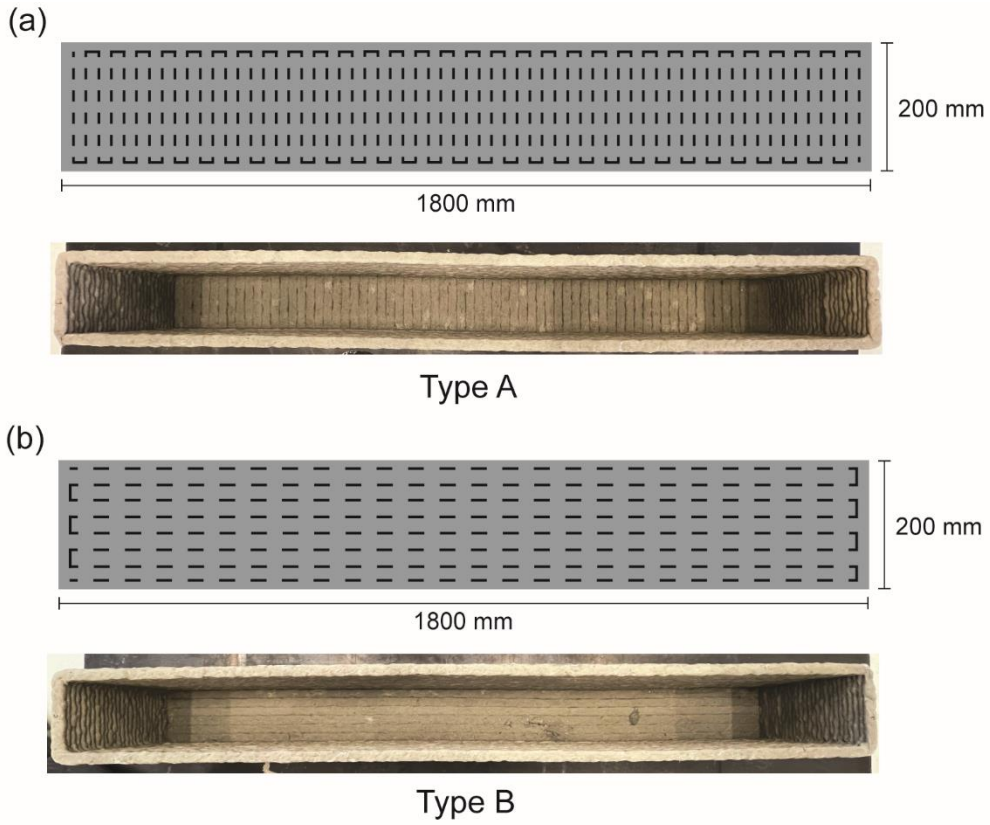

Figure 3. Printing patterns for the soffit of 3DP-EGC permanent formwork. The dotted line represents moving path of the printhead.

Preprints (www.preprints.org) | NOT PEER-REVIEWED | Posted: 30 March 2022 doi:10.20944/preprints202203.0390.v1

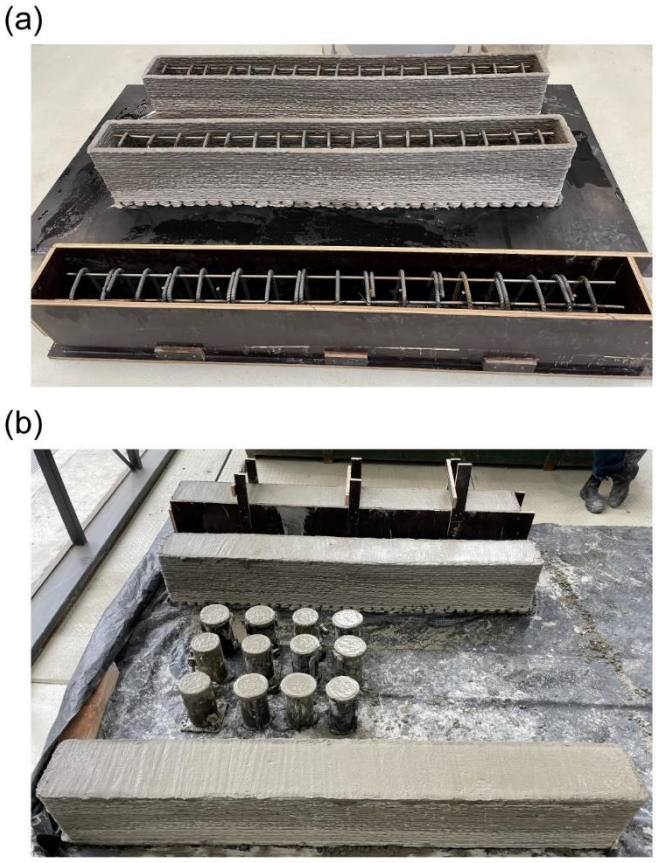

Figure 4. (a) Reinforcement cages were placed inside the 3DP-EGC permanent formwork and temporary formwork; (b) OPC concrete was cast inside the 3DP-EGC permanent formwork and the temporary formwork.

Preprints (www.preprints.org) | NOT PEER-REVIEWED | Posted: 30 March 2022 doi:10.20944/preprints202203.0390.v1

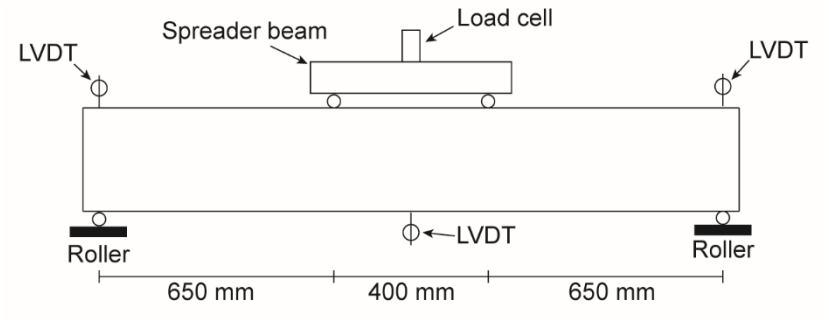

Figure 5. Four-point bending test setup.

Preprints (www.preprints.org) | NOT PEER-REVIEWED | Posted: 30 March 2022 doi:10.20944/preprints202203.0390.v1

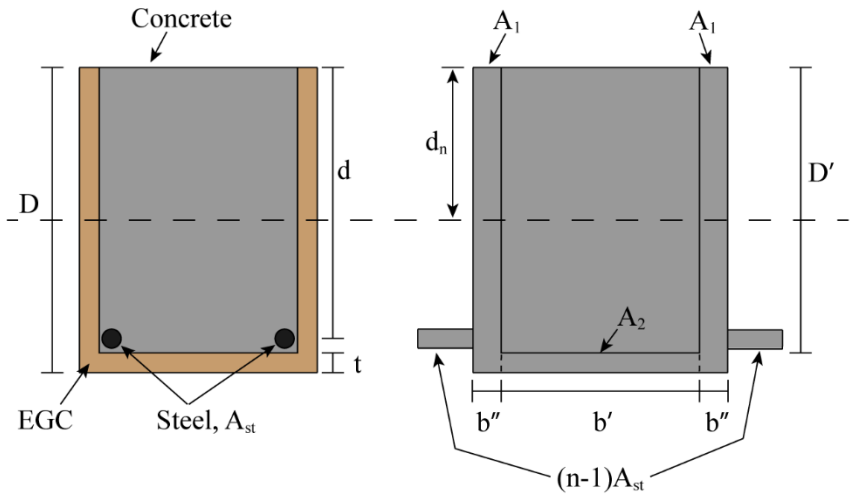

Figure 6. Transformed sections of steel and 3DP-EGC permanent formwork to an equivalent concrete area.

Preprints (www.preprints.org) | NOT PEER-REVIEWED | Posted: 30 March 2022 doi:10.20944/preprints202203.0390.v1

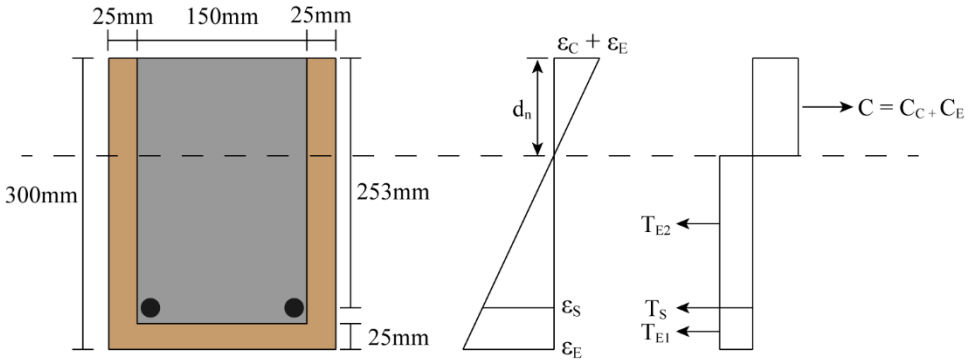

Figure 7. Stress and strain diagrams of the cross-section of RC beam made using 3DP-EGC permanent formwork.

Preprints (www.preprints.org) | NOT PEER-REVIEWED | Posted: 30 March 2022 doi:10.20944/preprints202203.0390.v1

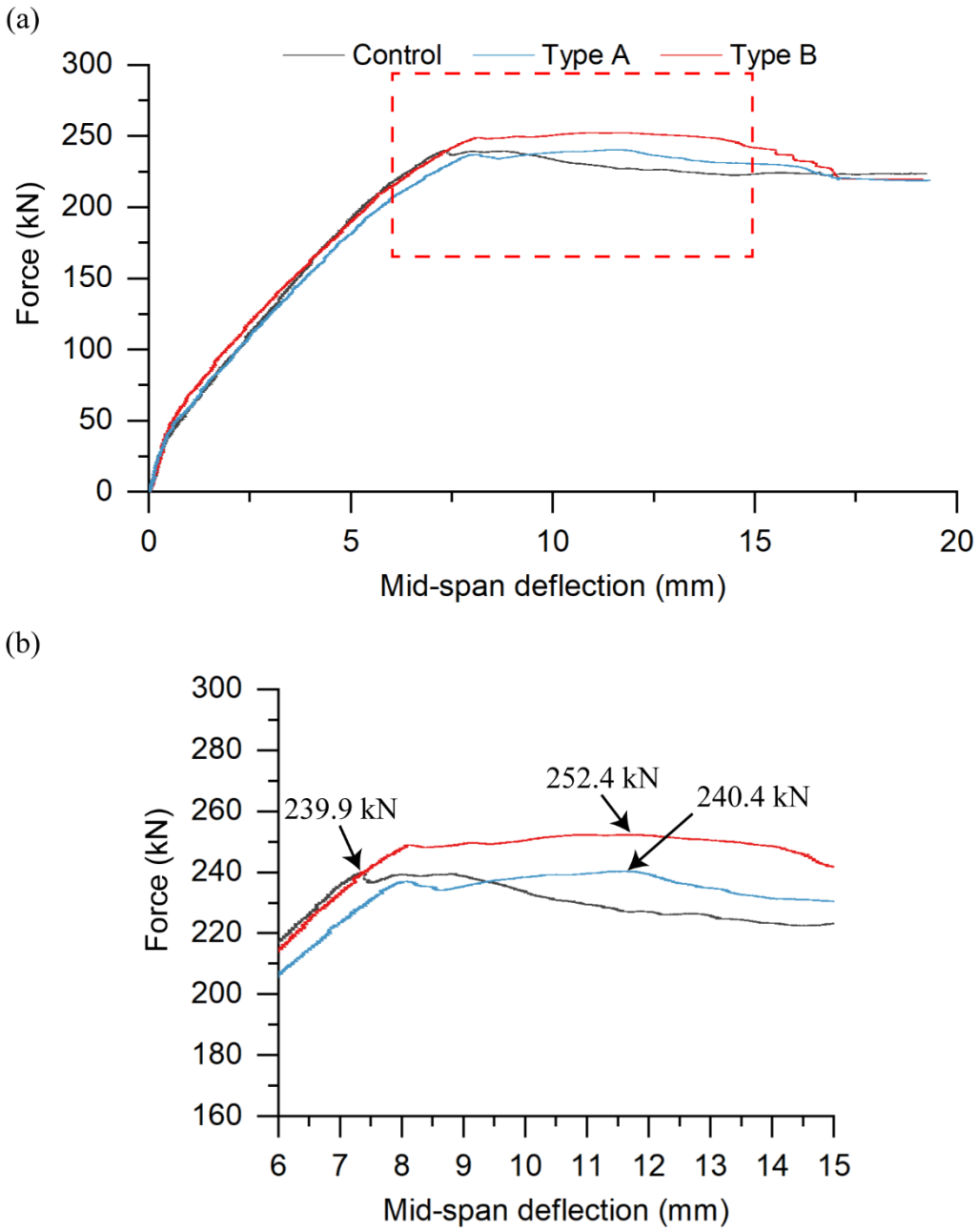

Figure 8. (a) Force vs. mid-span deflection curves of the RC beam specimens and (b) enlargement of the area shown in the red rectangle in (a) showing the ultimate forces of the RC beam specimens.

Preprints (www.preprints.org) | NOT PEER-REVIEWED | Posted: 30 March 2022 doi:10.20944/preprints202203.0390.v1

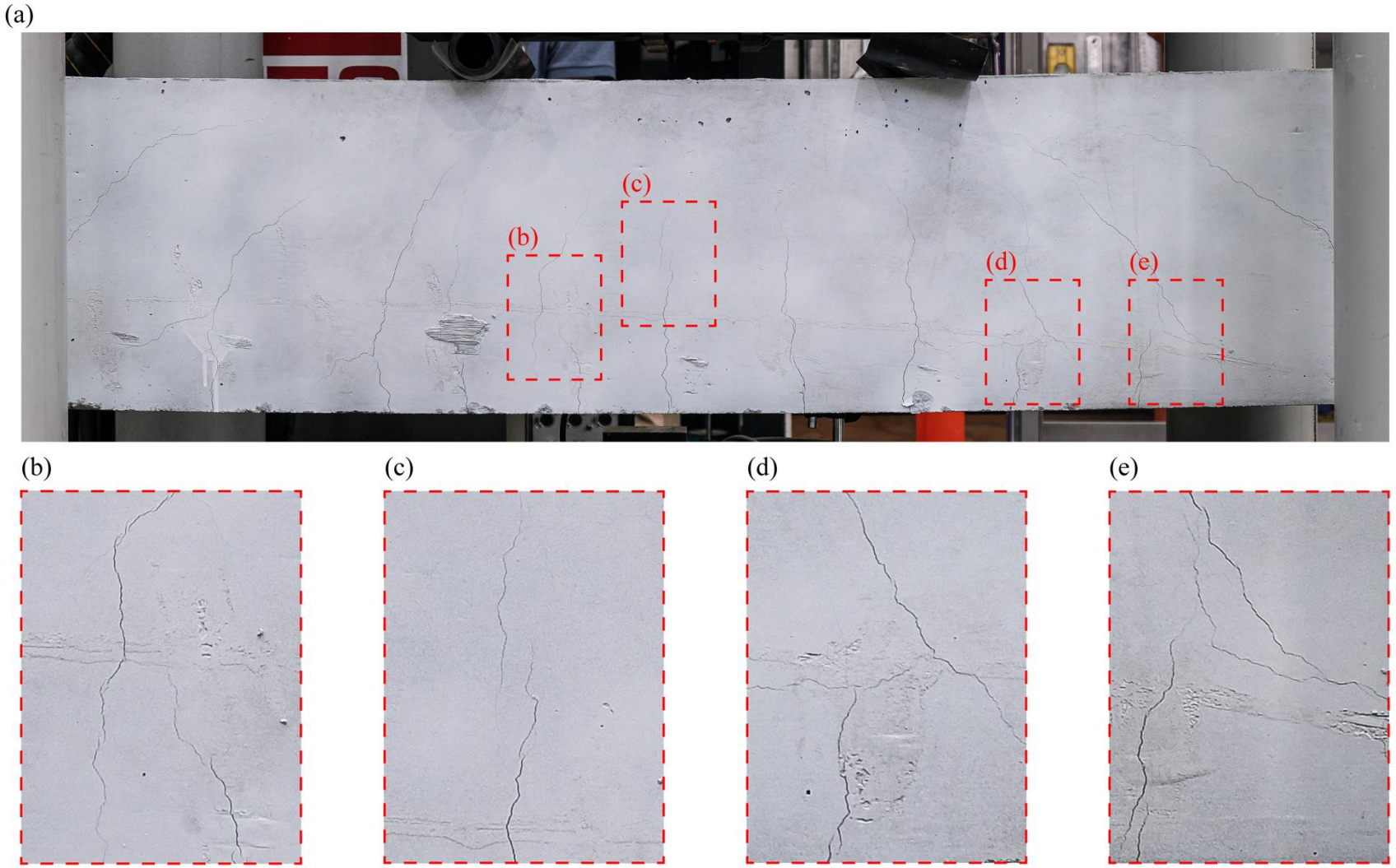

Figure 9. (a) Cracking pattern of the control beam at ultimate load and (b), (c), (d) and (e) 300% enlargement of the areas shown in the red rectangles in (a).

Preprints (www.preprints.org) | NOT PEER-REVIEWED | Posted: 30 March 2022 doi:10.20944/preprints202203.0390.v1

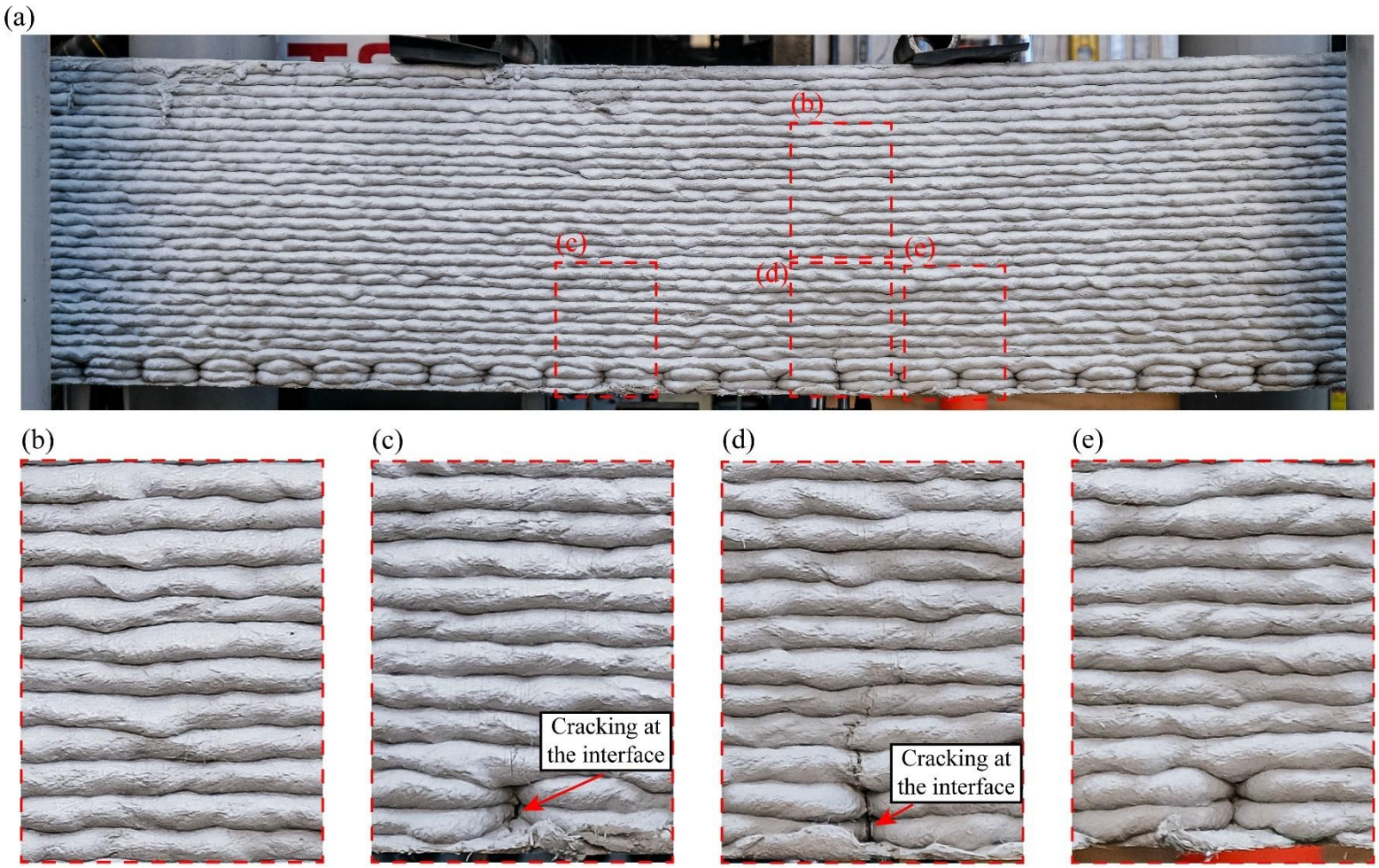

Figure 10. (a) Cracking pattern of Type A RC beam at the ultimate load, and (b), (c), (d) and (e) 300% enlargement of the areas shown in the red rectangles in (a) showing multiple fine cracks.

Preprints (www.preprints.org) | NOT PEER-REVIEWED | Posted: 30 March 2022 doi:10.20944/preprints202203.0390.v1

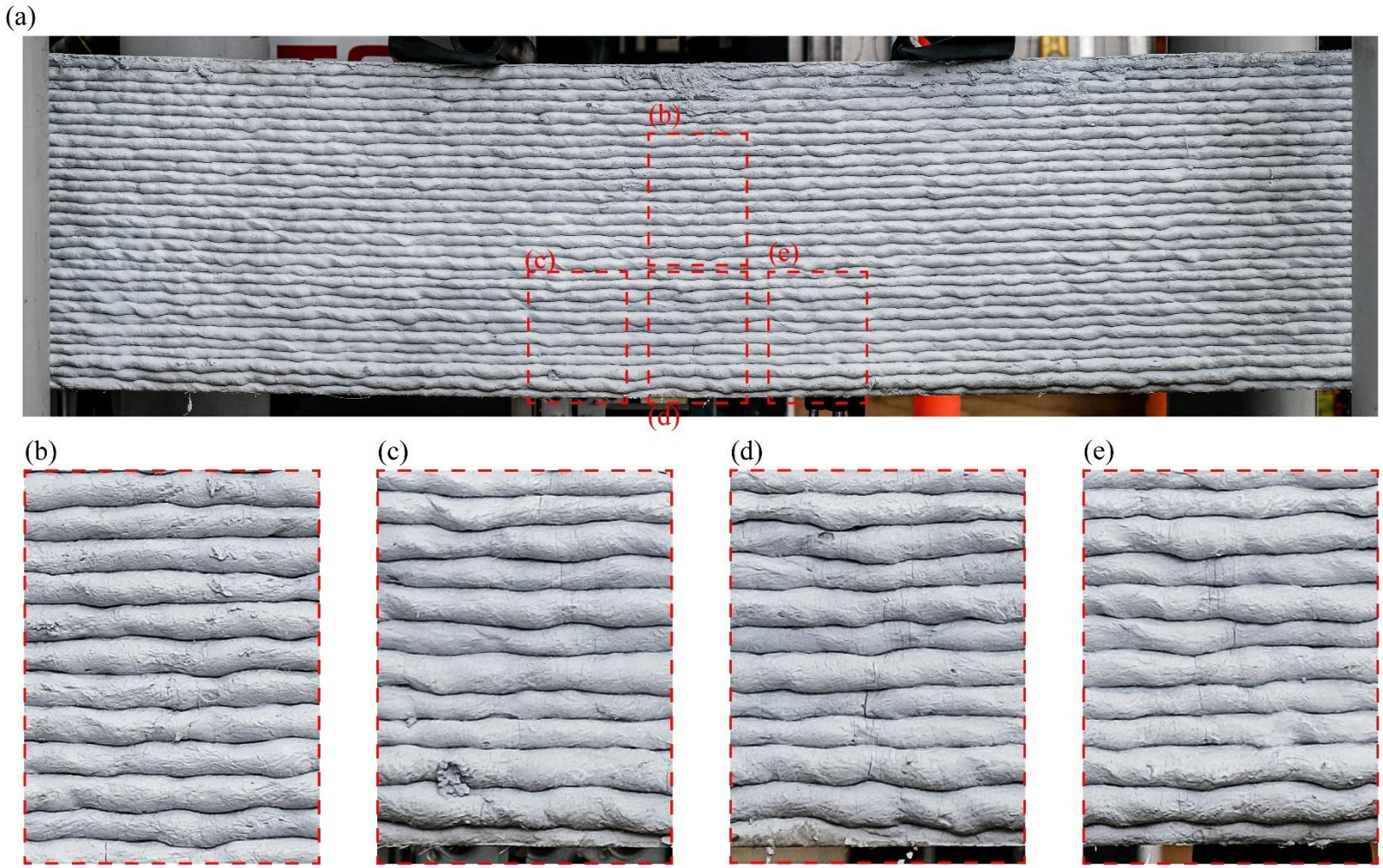

Figure 11. (a) Cracking pattern of Type B RC beam at the ultimate load, and (b), (c), (d) and (e) 300% enlargement of the areas shown in the red rectangles in (a) showing multiple fine cracks.

Preprints (www.preprints.org) | NOT PEER-REVIEWED | Posted: 30 March 2022 doi:10.20944/preprints202203.0390.v1

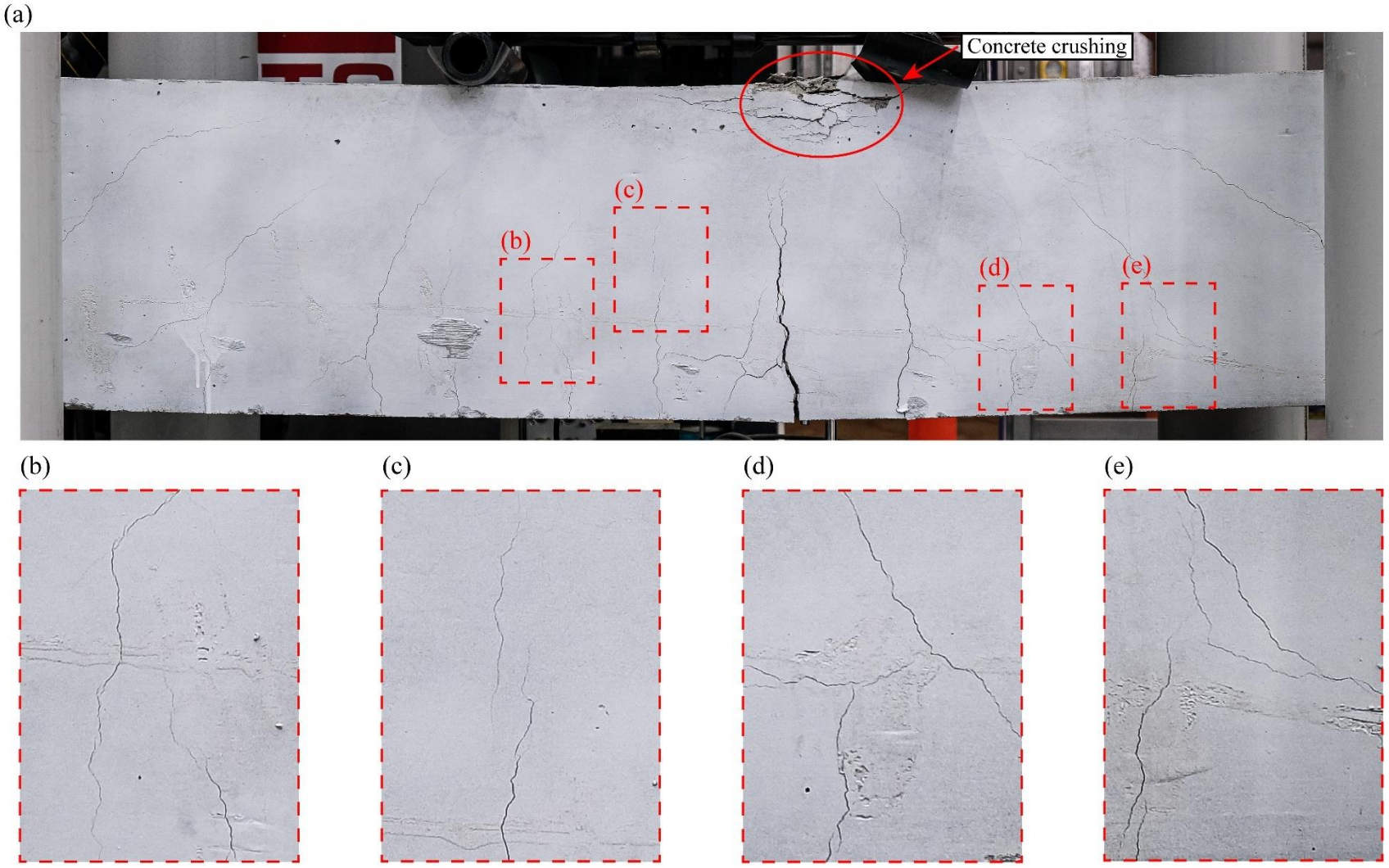

Figure 12. (a) Cracking pattern of the control beam at mid-span deflection of 16 mm, and (b), (c), (d) and (e) 300 % enlargement of the areas shown in the red rectangles in (a).

Preprints (www.preprints.org) | NOT PEER-REVIEWED | Posted: 30 March 2022 doi:10.20944/preprints202203.0390.v1

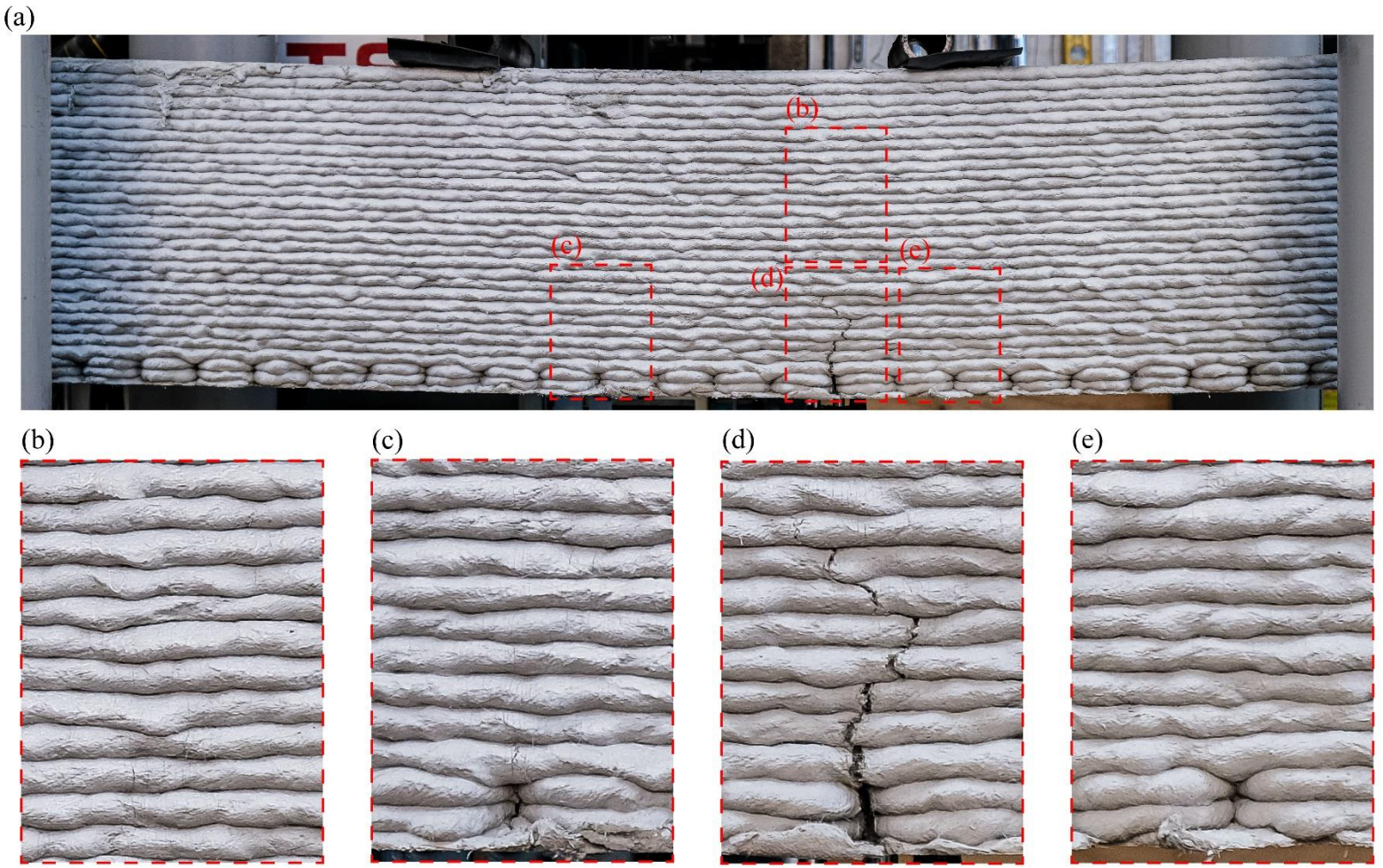

Figure 13. (a) Cracking pattern of Type A RC beam at mid-span deflection of 16 mm, and (b), (c), (d) and (e) 300% enlargement of the areas shown in the red rectangles in (a) showing multiple fine cracks.

Preprints (www.preprints.org) | NOT PEER-REVIEWED | Posted: 30 March 2022 doi:10.20944/preprints202203.0390.v1

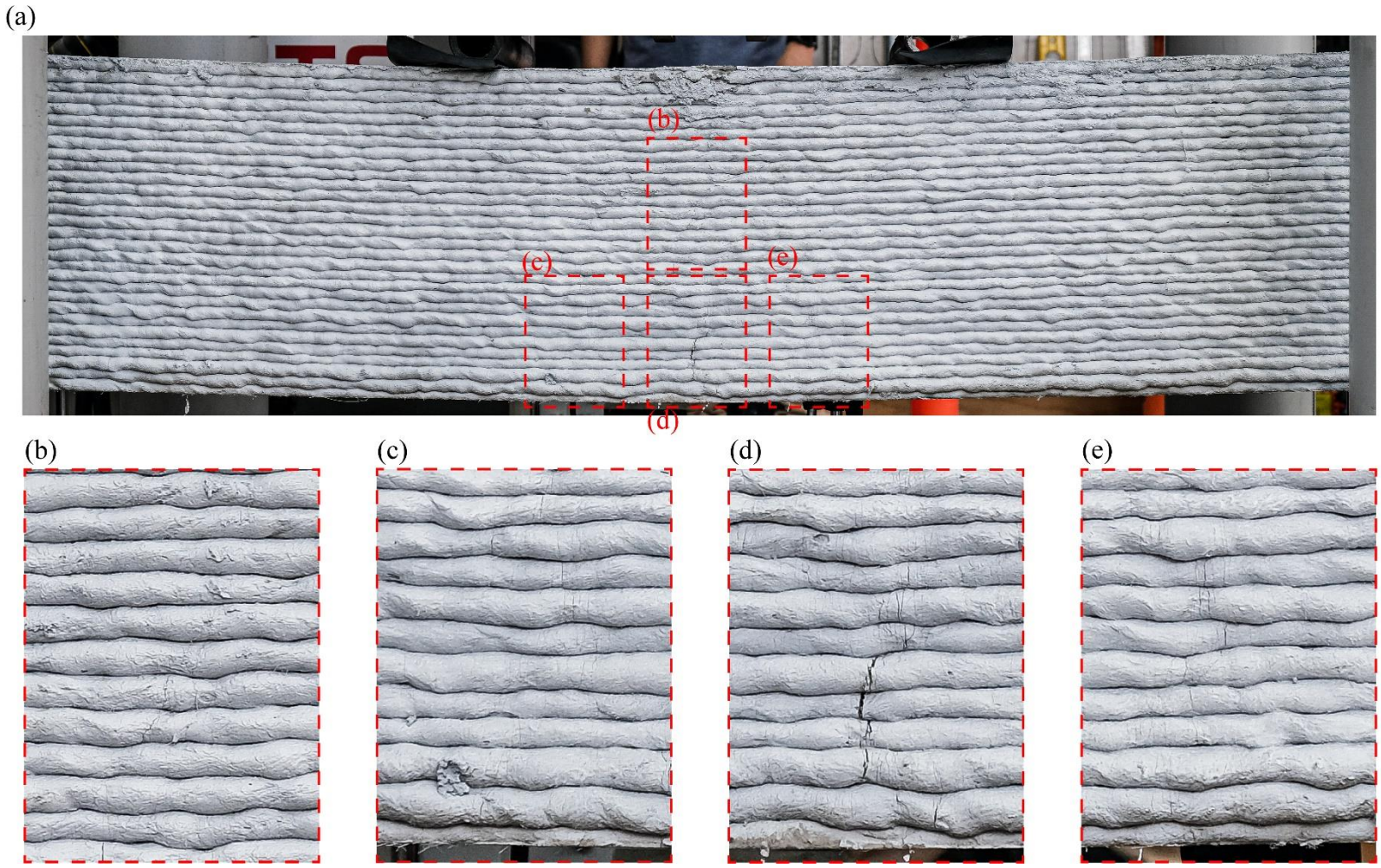

Figure 14. (a) Cracking pattern of Type B RC beam at mid-span deflection of 16 mm, and (b), (c), (d) and (e) 300% enlargement of the areas shown in the red rectangles in (a) showing multiple fine cracks.

Preprints (www.preprints.org) | NOT PEER-REVIEWED | Posted: 30 March 2022 doi:10.20944/preprints202203.0390.v1

Figure 15. Cracking pattern of the bottom side (tension region) of the RC beam specimens; the photos were taken after unloading.

Preprints (www.preprints.org) | NOT PEER-REVIEWED | Posted: 30 March 2022 doi:10.20944/preprints202203.0390.v1

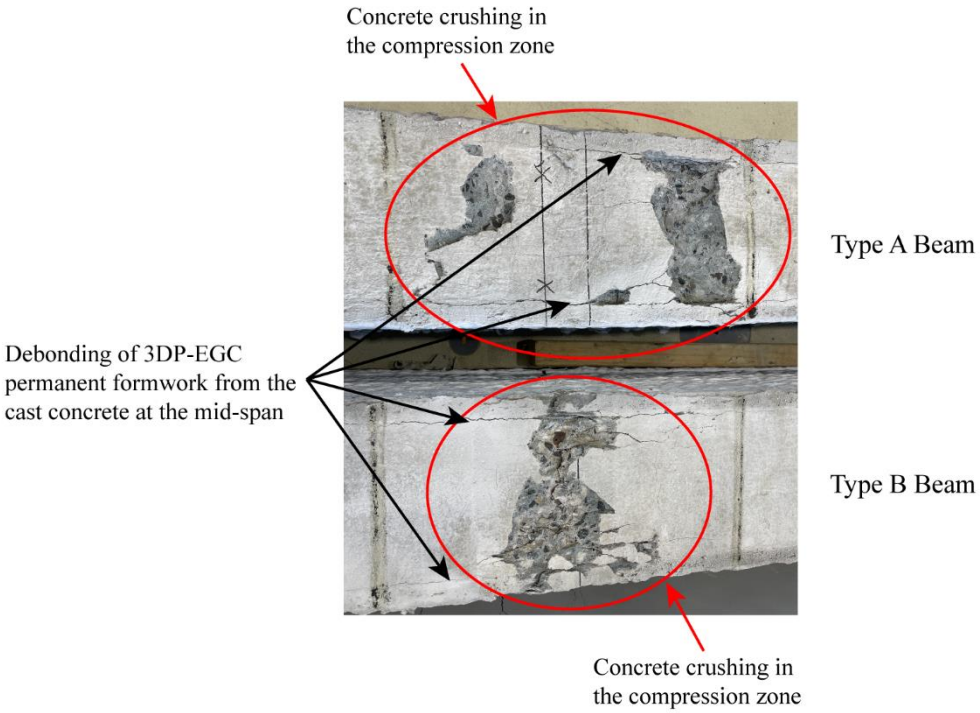

Figure 16. Debonding of the 3DP-EGC permanent formwork from the cast concrete in the compression zone at the mid-span; photos of the top views of beam specimens were taken after unloading.

 doi:10.20944/preprints202203.0390.v1

Table 1. Mechanical properties of 3DP-EGC and its counterpart mould-cast EGC at 28 days. Adopted from [16].

Mechanical properties	Mould-cast EGC	3DP-EGC
Average compressive strength	62.1 MPa	58.2, 53.6, 47.4 MPa[a]
Average density	1921 kg/m^3	1874 kg/m^3
Average modulus of rupture	6.9 MPa	8.0 MPa[b]
Average uniaxial tensile strength	3.4 MPa	3.8 MPa[c]
Average tensile strain capacity	2.1%	1.8%[c]

[a] Measured in longitudinal, lateral and perpendicular directions, respectively.
[b] Measured in perpendicular direction.
[c] Measured in longitudinal direction.

Preprints (www.preprints.org) | NOT PEER-REVIEWED | Posted: 30 March 2022 doi:10.20944/preprints202203.0390.v1

Table 2. Material characteristics used to calculate M_{cr}.

Concrete modulus of elasticity[1], E_c (MPa)	31,887
EGC modulus of elasticity[2], E_E (MPa)	17,835
Mean value of flexural tensile strength[3], MOR (MPa)	6.9
Characteristic flexural tensile strength[4], $f'_{ct,f}$ (MPa)	6.2
Steel modulus of elasticity, E_s (MPa)	200,000

[1] Derived in accordance with Clause 3.1.2 of AS 3600 [20].

[2] Derived in accordance with Section 3.4 of Recommendations for Design and Construction of High Performance Fibre Reinforced Cement Composites with Multiple Fine Cracks (HPFRCC) [22].

[3] Adopted from [16] for the ambient temperature cured mould-cast EGC.

[4] $f'_{ct,f}$=$MOR - 1.645 \times$(Standard Deviation), in accordance with Section 3.2.2 of Recommendations for Design and Construction of High Performance Fibre Reinforced Cement Composites with Multiple Fine Cracks (HPFRCC) [22].

Preprints (www.preprints.org) | NOT PEER-REVIEWED | Posted: 30 March 2022 doi:10.20944/preprints202203.0390.v1

Table 3. Material characteristics of EGC used to derive M_u.

Mean value of compressive strength[1], $f_{CE}^{'}$ (MPa)	62.1
Characteristic compressive strength[2], $f_{CEk}^{'}$ (MPa)	55.4
Mean value of ultimate tensile strength[3], σ_{ult} (MPa)	3.4
Characteristic ultimate tensile strength[4], f_{ultk} (MPa)	3.2
Material factor; γ_c[5]	1.3

[1] Adopted from [16] for the ambient temperature cured mould-cast EGC.

[2] $f_{CEk}^{'}=f_{CE}^{'}-1.645\times$(Standard Deviation), in accordance with Section 3.1 of Recommendations for Design and Construction of High Performance Fibre Reinforced Cement Composites with Multiple Fine Cracks (HPFRCC) [22].

[3] Adopted from [16] for the ambient temperature cured mould-cast EGC.

[4] $f_{ultk}=\sigma_{ult}-1.645\times$(Standard Deviation), in accordance with Section 3.2.4 of Recommendations for Design and Construction of High Performance Fibre Reinforced Cement Composites with Multiple Fine Cracks (HPFRCC) [22].

[5] According to Section 3.2.1 of Recommendations for Design and Construction of High Performance Fibre Reinforced Cement Composites with Multiple Fine Cracks (HPFRCC) [22].

 doi:10.20944/preprints202203.0390.v1

Table 4. Flexural test results of RC beam specimens.

Properties	Control beam	Type A	Type B
Cracking force, P_{cr} (kN)	38.2	42.2	54.5
Deflection at cracking force, δ_{cr} (mm)	0.5	0.6	0.7
Yielding force, P_y (kN)	203.4	198.7	206.6
Deflection at yielding force, δ_y (mm)	5.4	5.6	5.6
Ultimate force, P_{ult} (kN)	239.9	240.4	252.4
Deflection at ultimate force, δ_{ult} (mm)	7.3	11.6	11.7

Preprints (www.preprints.org) | NOT PEER-REVIEWED | Posted: 30 March 2022 doi:10.20944/preprints202203.0390.v1

Table 5. Comparison of measured and calculated cracking and ultimate forces of the RC beam specimens.

RC beam ID	Measured cracking force P_{cr} (kN)	Calculated cracking force $P_{cr.cal}$ (kN)	Ratio $P_{cr}/P_{cr.cal}$	Measured ultimate force P_{ult} (kN)	Calculated ultimate force $P_{ult.cal}$ (kN)	Ratio $P_{ult}/P_{ult.cal}$
Control	38.2	39.8	0.96	239.9	221.3	1.08
Type A	42.2	52.0	0.81	240.4	242.4	0.99
Type B	54.5	52.0	1.05	252.4	242.4	1.04

 doi:10.20944/preprints202203.0390.v1

Table 6. Ductility index and absorbed energy of RC beam specimens.

RC beam ID	Ductility index	Absorbed energy (kJ/m^2)
Control	1.4	1,046
Type A	2.1	2,026
Type B	2.1	2,162